Tests and characterisations of the ALPAO 64x64 deformable mirror, the MICADO-MAORY SCAO AIT facility

Fabrice Vidal, Jordan Raffard, Eric Gendron, Simone Thijs, Vincent Lapeyrère, Jean-Tristan Buey, Yann Clénet, Damien Gratadour, Pascal Jagourel, Arnaud Sevin, et al.

Tests and characterisations of the ALPAO 64×64 deformable mirror, the MICADO-MAORY SCAO AIT facility

F. Vidal[a], J. Raffard[a], E. Gendron[a], S. Thijs[a], V. Lapeyrere[a], T. Buey[a], Y. Clénet[a], D. Gratadour[a], P. Jagourel[b], A. Sevin[a], F. Ferreira[a], F. Chemla[b], and P. Mahiou[c]

[a] LESIA, Observatoire de Paris, Université PSL, CNRS, Sorbonne Université, Université de Paris, 5 place Jules Janssen, 92195 Meudon, France

[b] GEPI, Observatoire de Paris, PSL Univ., CNRS, 5 Place Jules Janssen, 92190 Meudon (France);

[c] ALPAO, 727 rue Aristide Bergès, 38330 Montbonnot-Saint-Martin (France)

ABSTRACT

MICADO is the ELT near-infrared first light imager. It will provide diffraction limited images using the single-conjugate adaptive optics (SCAO) mode developed inside the MAORY AO module. Although the MICADO-MAORY SCAO mode uses during regular operations the ELT wavefront correction capabilities (M4 & M5 adaptive mirrors), the SCAO system will not be able to work with them until the final instrument commissioning. Since it is crucial to test and validate the SCAO system during various AITs phases in Europe, the need of a high order deformable mirror with comparable number of degrees of freedom is required to test both spatial and temporal behaviour of the SCAO mode.

For that purpose, the SCAO AITs in Europe will use the newly developed ALPAO 64×64 actuators deformable mirror (DM). Before using this deformable mirror in the context of the SCAO mode (i.e controlled by a non-linear pyramid WFS, we built a classical Shack-Hartmann WFS to ensure a proper linear wavefront measurement in the lab and perform the DM characterisation of its 3228 actuators. We present the preliminary results of the tests performed on this DM in a classical closed loop scheme. In particular we study the spatial wavefront correction, actuators additivity and linear response, maximum amplitude range (stroke), hysteresis and temporal stability.

Keywords: Deformable Mirror, ELT

1. INTRODUCTION

Deformable mirrors (DM) are commonly used in Adaptive Optics (AO) to perform turbulence wavefront correction enabling high angular resolution for ground based telescopes. The need of a high number of actuators is nowadays driven by the increase of telescope size such as the next generation of Extremely Large Telescopes (ELTs) and performance improvement of the current high contrast imaging AO instruments.

MICADO is the near-infrared first light imager for the European ELT.[1] It will provide diffraction limited images with a dedicated Single Conjugated AO (SCAO) module using a pyramid wave-front sensor[2] (PWFS) and the telescope built-in deformable mirror: the so-called M4 DM. The latter being only available during the final commissioning of the system in Chile, the various AITs in Europe will therefore need an equivalent wavefront corrector with a similar number of degrees of freedom for the tests and validations.

For that purpose the SCAO system (i.e the WFS path) features a calibration unit (SCU) to emulate the turbulence, the pupil shape, and the M4 deformable mirror during AITs in Europe. It will make it possible to close the loop with similar conditions from those encountered at the ELT and characterize the spatial and temporal behavior of the AO system. To emulate M4 it is decided to use the newly developed deformable mirror 64×64 actuators by ALPAO[3] as a test facility for MICADO SCAO.

Further author information: (Send correspondence to Fabrice Vidal: E-mail: fabrice.vidal@obspm.fr, Telephone: +33 (0)1 45077942

2. DM SPECIFICATIONS

The ALPAO DM features 3228 actuators across a circular full aperture of 96 mm distributed on a 64×64 regular square pattern (inter-actuator pitch of 1.5 mm). Table 1 summarises the main relevant DM specifications.

Parameter	**Value**
Total number of actuators	3228
Nb of actuators across the diameter	64
Full aperture	96 mm
Useful aperture (pupil)	93.5 mm
Mechanical stroke	$>3.5\mu$m
Inter-actuator mechanical stroke	$>1.2\mu$m
Actuator hysteresis	$<2\%$
Electronics protocol	10Gb up to switch then 1Gb
Command encoding	14 bits

Table 1: Summary of the main ALPAO 64×64 specifications.

3. BENCH SETUP

A dedicated test bench was used to test the deformable mirror. It uses a classical 85×85 Shack-Hartmann (SH) with 8×8 pixels per sub-aperture located in front of the deformable mirror. Table 2 summarises the characteristics of this SH WFS. We did not use any turbulence simulator since measuring the DM characteristics does not necessarily imply to be in close loop scheme (it is actually preferred to be in open loop). It is also important to notice that the Shack-Hartmann was calibrated beforehand to ensure that the linearity of the measurements in the requested dynamic range (i.e stroke of the DM) is always valid. We estimate the wavefront measurement accuracy of the SH at a level smaller than <7 nm rms. The DM electronics are controlled with a classical computer (not real time). The commands can potentially be sent and received as fast as $\approx$ 2 Khz. However the actual speed limitation is due to the frequency of the camera (25 Hz) and to some synchronisation and software limitations that ensures the freshness of the wave-front measurement. This eventually leads to measurements performed at $\approx$ 3 Hz. The spatial sampling of the DM surface by the SH is not sufficient enough to characterize the DM influence functions in detail. However we plan for future tests to use a pyramid WFS with a 240×240 measurement points per pupil diameter to characterize the DM influence functions into more details. Furthermore the current capabilities of the bench did not allowed us, at least for this paper, to characterize the temporal behavior of the DM (actuators rising time, overall DM bandwidth, etc.). This activity is planned for the future by using stroboscopic capabilities synchronized with the DM commands. Figure 1 shows the ALPAO DM installed in our test lab.

Parameter	**Value**
Pixel size	6.45 μm
Micro-lens focal length	480 μm
Number of micro-lenses	85×85 (5449)
Micro-lens pitch	55 μm
Focal length of collimator	75 mm
Sensitivity	739 nm/pixel/μlens

Table 2: Optical and physical design parameters of the Shack-Hartmann used for the characterisation of the DM.

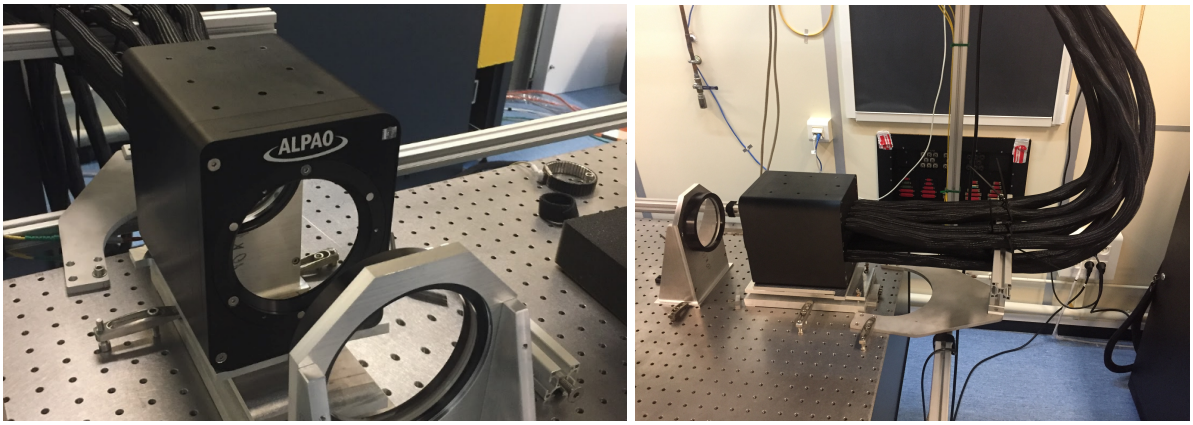

Figure 1: The ALPAO 64×64 DM installed in the lab, ready for the tests.

4. CALIBRATIONS

4.1 Modes computation

The first calibration step is to define a set of modes that will be used to control and characterise the deformable mirror. First the set of coordinates of all the actuators is identified (taking care of ordering them properly) as a set of points A_k in the pupil, with $k \in [0, N_{act}[$. The covariance matrix of the phase was computed for the positions of the A_k, ignoring any kind of influence function. Then the piston mode is filtered out from this matrix (a pure piston with phase values all equal). The matrix was finally diagonalised, leading to some eigenvectors forming the modes. The Fourier transform of any of these modes shows only a unique spatial frequency. It may have any arbitrary directions, but the modulus of its frequency components is unique per mode.

4.1.1 Why are modes *monochromatic* ?

This matrix is a discrete convolution matrix, because of the spatial stationarity of the phase. It is known that the eigenmodes of a convolution are sine and cosine modes: indeed any sine wave remains a sine wave after convolution by any kernel, and keeps the same phase when the kernel is symmetric. For that reason, the eigenvalues reflect the attenuation of the spatial frequency after convolution: consequently they are the transfer function, i.e. the Fourier transform of the convolution kernel. This latter is in our case the covariance of the phase and it is known that its Fourier transform is the Kolmogorov spectrum of the turbulence ; that is why the modes are the Karhunen-Loeve modes of the atmosphere, with eigenvalues decreasing as the turbulent spectrum. Diagonalisation also reveals groups of degenerate modes, that form subspaces with identical eigenvalue for any of its vector. A basis of those subspaces is simply the set of sine waves with identical spatial frequency, and arbitrary direction. That last statement is the point we want to emphasize: modes are necessarily *single-frequency* ones (in norm, not direction). Their Fourier transform is necessarily a circle (because the properties of the phase are spatially isotropic).

4.1.2 Producing the modes with a DM

As expected, one of the eigenvalues is null and corresponds to the filtered piston mode. All the others modes are then orthogonal to piston (using a scalar product in command space). The first modes exhibit tip and tilt-like modes, then defocus and astigmatisms, etc. necessarily sorted by increasing spatial frequency according to Kolmogorov (or Von Karman) spectrum with the piston coming at the very end just after a series of waffle-like modes. Computed as such, those modes are independent from the DM properties, as they have been computed ignoring entirely the actuator influence functions. This ensemble of vectors forms anyway a basis of the DM command space, and has particular properties. First,

$$B^t\, B = B\, B^t = \mathrm{Id} \tag{1}$$

Second, we assume that the influence function is the same for any actuator. Producing a given mode with the DM amounts to immerse the discrete spatial representation of the DM into the real continuous space and convolve it with the influence function. Ignoring aliasing and edge effects, this operation will not modify the shape of the mode because each of them is spatially *monochromatic*.

Proceeding that way offers a computationally light way to compute spatially ordered modes of the DM that inherently match the Karhunen-Loeve (KL) modes (the KLs within the DM space, not the atmospheric KL projected onto DM subspace and that might not be orthogonal), featuring quasi-tiptilt as low order modes, then astigmatism, defocus etc. and finishing with waffle-like modes.

4.2 Interaction matrix

4.2.1 Sinus method and demodulation

The algorithm used to make the interaction matrix consists in dithering each mode of the basis using a sinusoidal excitation, at a frequency specific to each mode. The frequency and the number of samples n over which the data recording is performed is such that all the modal dithering signals will be orthogonal to each others. Technically, this is obtained first by choosing the dithering signals $d_k(t)$ such as:

$$d_k(t) = a_k \sin(2\pi f_k t/n) \tag{2}$$

with t, f_k, and n all integers. The variable t stands conceptually for the time but is an integer value that represents in the reality the frame number, and is restricted to the range $t \in [0, n[$. The variable f_k is the *frequency* associated to mode number k. Again, the term *frequency* is just conceptual here. The value of f_k shall be an integer one: it is the number of dithering cycles the mode will undergo during the n record samples. The sine waves shall be sufficiently well sampled, which requires to have $n > 2f_m$ (m is the number of modes, i.e. f_m is the maximum frequency. For safety, we prefer to take some margin on that condition and choose the number of samples n so that:

$$n = 3\, f_m \tag{3}$$

We propose several ways of selecting the frequencies f_k. The most natural one that has been chosen for our tests is to set

$$f_k = f_0 + k\,,\; k \in [0, m[\tag{4}$$

with the value of f_0 being an arbitrary integer. The choice of f_0 shall be driven by the real physical value of the frequency F_0 (that one is the real frequency, in Hz) associated to f_0, that shall keep away from the low-frequency regime of the turbulence of the laboratory or telescope. We typically want to have $F_0 > (1-10)$Hz. In order to compute it, one has to take into account the frame period T_e (or the frame frequency F_e) in order to compute the slowest sine wave period : $T_0 = 3(m+f_0)T_e/f_0$, or its frequency:

$$F_0 = \frac{f_0}{3(f_0+m)} F_e \tag{5}$$

which can be solved to get the value of f_0 as a function of the desired F_0:

$$f_0 = \left\lfloor \frac{m}{\frac{F_e}{3F_0} - 1} \right\rfloor \tag{6}$$

with $\lfloor ... \rfloor$ that denotes the integer part.

Others ways of selecting the frequencies may be of relevance. Let us notice that harmonics can arise from non-linear behaviour either from the DM or from the sensor. Quadratic, cubic behaviours will induce some doubling or tripling of the frequency so that when a frequency f_k has been chosen, one shall skip its multiples $2f_k$, $3f_k$, etc. This allows all integers from f_0 to $2f_0 - 1$ and then the choice rapidly narrows and reduces to primary numbers.

Let us call V the matrix of size (m, n) (an horizontal collection of column-vectors of modal coefficients) with the coefficient v_{kt} defined as:

$$v_{kt} = a_k \sin(2\pi f_k t/n) \tag{7}$$

The matrix V contains the temporal dithering signal of mode k at line number k. Let us call D the interaction matrix of the sensor. Let us call S the set of wave-front slopes measurements provided by our sensor, of size (p, n) (an horizontal collection of n column-vectors of length p of slopes measurements). Those three matrices are linked by the relation:

$$S = D.V \tag{8}$$

We assume that we are able to apply on the DM at each frame a new column-vector of V and we place the associated measurement in S. The matrices S and V are known, we shall now find D.

Due to the orthogonality of the dithering signals the matrix V has the remarkable property:

$$V.V^t = \frac{n}{2}\,\mathrm{Diag}(a_k^2) \tag{9}$$

where $\mathrm{Diag}(a_k^2)$ is a diagonal matrix made by the square amplitudes of the sine waves a_k^2. The interaction matrix D can be solved from Eq. 8 by writing:

$$D = \frac{2}{n}\,S.V^t.\mathrm{Diag}(a_k^{-2}) \tag{10}$$

This operation consists in projecting the measurements onto the dithering sine waves for demodulation. It is equivalent to a Fourier transform made by matrix product, and computed uniquely for the particular and exact dithering frequencies and, more importantly, with the proper phase.

4.2.2 Discussion

Eq. 10 can be written for any V that fulfills Eq.9, and our method applies thanks to that equation. Sine waves do the job, but any other orthogonal set of signals would do as well. For instance, the Hadamar matrices[4,5] are an example of such orthogonal signals, particularly efficient as the poke amplitudes are only $\pm a_k$ and using a number of samples n equal to the number of actuators. For those who would like to apply normally-distributed signals, it is possible to generate random signals made orthonormal through a Gram-Schmidt orthonormalization for instance. The choice for the orthogonal signals is virtually unlimited and can be adapted to the particular case of each user.

We have chosen sine waves first because they are quite simple to implement, and because we think it is important to master the temporal frequency range where the DM pokes are applied, in order that the demodulation process (i.e. the multiplication by V^t) rejects best the perturbations coming from the lab environment.

4.2.3 Variation using sine and cosine

A refinement of the method consists in using the dithering signal

$$\begin{cases} d_{2k} = & a_k \cos(2\pi f_k t/N) \\ d_{2k+1} = & a_k \sin(2\pi f_k t/N) \end{cases} \tag{11}$$

for the modes number $2k$ and $2k+1$. Although at the same frequency, those signals are in quadrature and still strictly orthogonal over the n samples of observation. This allows us to get a factor of 2 on the number of frequencies to be employed, i.e. nearly a factor of 2 on the calibration time. Although apparently efficient, we recommend to restrict the use of that method to laboratory experiments only that do not have to deal with latency issues between the DM voltage application and measurement. While a time shift in the measurements has virtually no impact when dealing with individual frequency per mode, some variable latency or jitter would compromise the results in this case.

5. RESULTS

5.1 DM stroke

5.1.1 Hardware limitations

The definition of the DM stroke is more subtile than with many other devices, because the command $\vec{v} = \{v_i\}$ is hitting against two limitation thresholds, that are

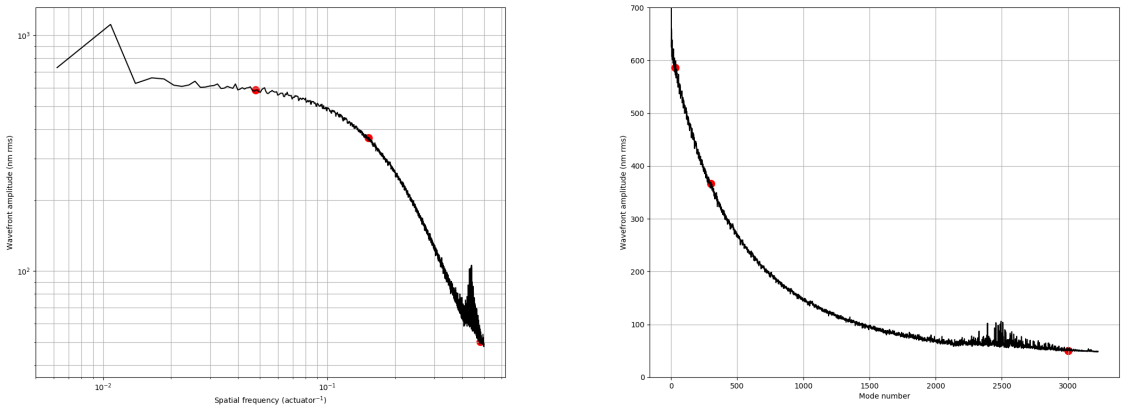

Figure 2: Value of the rms wavefront amplitude (in nm rms) for each mode or our modal basis with a unitary command energy in log-log (left) or lin-lin (right). The result is plotted against the spatial frequency of the mode expressed in act^{-1} on the left, or against the mode number of the right. Modes 30, 300 and 3000 are shown with a red dot.

- $-1 < v_i < 1$
- $\sum v_i^2 < E$; with $E = 80$ (power limit given by ALPAO).

First the command vector must always be set in the range $[-1, 1]$ (unitless number) because the motion of a single actuator is limited, but also the sum of squares of the actuator commands must be lower than a software factory-defined limit, set to 80 in our case and related to the maximum power that can be delivered by the electronics.

5.1.2 Notion of *command energy* ; DM transfer function

Let $\vec{v} = \{v_i\}$ be a unitary command vector, i.e. such that

$$\sum_i v_i^2 = 1 \ . \tag{12}$$

We will call *energy* of a command vector the sum of the squares of the actuator values. The rms amplitude of the wavefront produced by the unitary energy command vector $\vec{v}$ on the DM is a function of the spatial frequency. Due to the spatial extension of the influence function (i.e. due to coupling between actuators), large amplitudes at low spatial frequencies can easily be produced because of the constructive addition of the membrane deflection. At the opposite, high spatial frequencies require more stroke in order to fight against the coupling between actuators. Because of our choice of orthogonal modes (as defined by Eq. 1), they all carry a unitary command energy, and the energy of a linear combination of modes is the sum of the individual energies. Using the interaction matrix of the modal basis, we were able to reconstruct the wavefront for each mode and measure the wavefront variance. Because our modal basis is also ordered by spatial frequency, we are able to plot the wavefront rms amplitude of the modes against their spatial frequency. This is represented on Fig. 2. We have chosen to express the spatial frequency in act^{-1} (as an example to illustrate our purpose, a frequency of 0.1 act^{-1} is a wave with a spatial period of 10 actuator pitch).

The Fig. 2 can be interpreted as the modulus of a transfer function, since it describes how the unitary spatial frequencies can be produced by the DM. It clearly shows a low-pass filter, which shape is actually the Fourier transform of the influence function. The two first modes are tip and tilt ; they somewhat differ from the rest of the plot for a reason that still to be investigated. Around 0.44 act^{-1} the plot shows an "accident" that has to see with the aliasing of both the DM and our Shack-Hartmann, and that we leave apart from that article. For

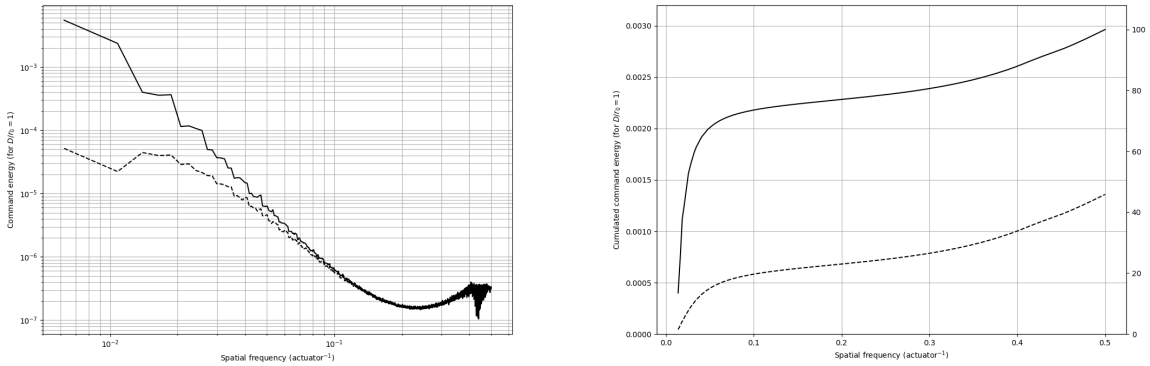

Figure 3: Amount of energy required for compensating the atmospheric turbulence with $D/r_0 = 1$ at 500 nm. The plain line is for an infinite outer scale ($D/L_0 = 0$). The dashed line is for $D/L_0 = 1.56$ (representing the ELT case with $D = 39$ m and $L_0 = 25$ m). This command energy is plotted against the spatial frequency of the modes. On the right, the values have been cumulated, started at mode number 3 (i.e. excluding tip and tilt). Units of vertical axis is average command energy (sum of squared actuator commands).

the first ≈ 100 modes, up to a frequency of 0.05 act^{-1}, a roughly constant value of 600 nm rms of OPD (optical path difference) is produced for a unitary command energy. Then the transfer function decreases and ends up at the maximum frequency of 0.5 act^{-1}, that corresponds to a period of 2 actuators in push-pull: this is the waffle mode. The sensitivity there is 50 nm rms, i.e. a factor of 12 below the first low order modes.

That transfer function allows us to understand how the DM stroke will be used for compensating atmospheric turbulence in the next section.

5.1.3 Compensation of turbulence

In order to know what is the amount of energy that is spent at compensating turbulence per spatial frequency, we can divide the spectrum of turbulence by the square of the previous transfer function. The result is shown on Fig. 3 (left), for a fully developed Kolmogorov turbulence. It shows that most of the energy is required from the low order modes, while the higher orders modes roughly require the same amount after ≈ 0.1 act^{-1} (i.e. after $\approx 100^{th}$ mode). On the right of Fig. 3 the same curve has been plotted, cumulating the energy values over the modes, and starting the integration at defocus mode (i.e. excluding the tip and tilt). The total required energy for $(D/r_0) = 1$ at 500 nm is $E_0 = 0.003$ when $L_0 = \infty$, or $E_0 = 0.00136$ when $L_0 = 25$ m on a 39 m ELT.

The result is that under fully developed Kolmogorov turbulence, the first 50 modes (tip-tilt excluded) require 70 % of the command energy, the 3175 others being the remaining 30%. It is likely that if potential saturations of the DM occur, they will be induced by the saturation of low-order modes rather than higher order ones.

The peak command energy the electronics can deliver is $E = 80$. We estimated that the maximum average energy compatible with this peak value and a saturation probability smaller than 0.01 shall be a factor of 3 below the peak, i.e. $E_{\text{average}} < 27$. It follows that the maximum (D/r_0) value ensuring "no" saturation is found following that equation:

$$\frac{D}{r_0} < \left(\frac{D}{r_0}\right)_{\max} = \left(\frac{E_{\text{average}}}{E_0}\right)^{3/5} \tag{13}$$

which gives $(D/r_0)_{\max} = 235$ at 500 nm. On a 39m telescope, this would set the limit where the DM occasionally begin to saturate 1% of the time to $r_0 = 16.6$ cm. This scales to $r_0 = 3.4$ cm on a 8 m telescope. Table 3 summarize the correctable turbulence depending on the telescope size and the fraction of which the DM will saturate.

D	L_0	$< 1\%$ sat.	10% sat.
39 m	∞	16.6 cm	11.0 cm
39 m	25 m	10.3 cm	6.9 cm
8 m	∞	3.4 cm	2.3 cm

Table 3: The table gives the r_0 values that are compatible with the use of the DM for various telescope sizes D and values of the outer scale L_0.

5.2 Modal interaction matrix

Considering Eq. 5, it is clear that the frequency F_0 is lower when m increases. Not surprisingly, the total time required for calibration increases while the value of F_0 gets smaller. Using $m = 3228$ actuators with a rather low frame rate, in our case $F_e = 3$ Hz, gives F_0 of the order of 0.01 Hz which is definitely too low even for a laboratory setup. We modify the calibration scheme that consists in splitting the DM calibration in several parts by splitting the modal basis in a number of blocks that will be calibrated one after the other. The previous equations still apply, provided m is replaced by the number of modes in each block.

We decided to use blocks of 150 modes which requires 500 WFS measurement frames per block. Therefore 22 blocks are required for calibrating all the mirror modes I.e 11000 WFS frames. A the current frequency of 3Hz this leads to a total interaction matrix calibration time of 1 hour. We also choose to reduce gradually the amplitude of sine waves with spatial frequencies order. The first block of 150 modes used a 2000 nm rms amplitude while the last 150 high order modes were calibrated with only 200nm rms amplitude.

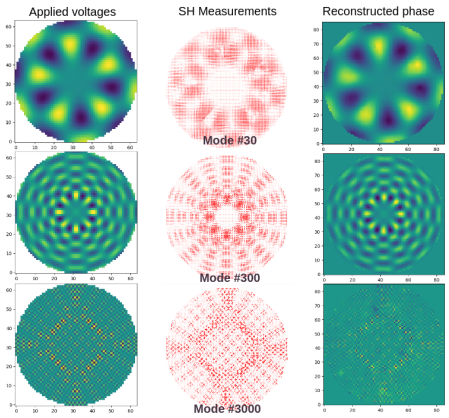

Figure 4: Example of generated DM voltages (left), measured by the SH (center) and reconstructed phase (right) for modes 30, 300 and 3000.

5.3 Unimodal linearity

The linearity of the DM motion with respect to an input modal poke has been tested by ramping up the voltage applied to a given mode from -1 to +1 (command energy units). A linear regression is applied to the measurements, and the ensemble of regression coefficients forms the reference modal measurement (applied iteratively to all modes, this could be another way to build an interaction matrix). What we want to study here is the accuracy of that linear motion for any point of the DM surface. For doing that, the set of measurements are projected (scalar product) onto the regressed modal measurement previously found, and a unique number is derived for each step of the ramp, that correspond to the amplitude of the measured mode.

Subtracting the raw measurements data to the product of the regressed modal measurement and its amplitude would tell us the amount by which the mode produced by the DM distorts with amplitude. But we want to do more, and also want to check how much it deviates from linearity against the input command. So, the amplitude previously found is adjusted by a linear regression with respect to the values of the command ramp, and we finally compute the error between the raw measurements data, and the product between that linear fit and the

modal measurements. The rms value (along the ramp) of this error is computed for each measurement (for each slope of the Shack-Hartmann) and the maximum of its value is deduced.

We found for all modes a result below 10 nm rms. The linearity is excellent, and the error is hardly above the capacities of our wave-front sensor. We also display as a bidimensional map the spatial distribution of the error and check whether this is incoherent or if it is actually related to the mode applied. The latter case is true: the signature of the mode appears in the error, which is the evidence that we actually measure a non-linearity error and that the method is valid.

As an example, a set of ramp voltage is applied on low (#30), medium (#300), and high order modes (#3000) which –according to Fig. 2– leads respectively to ±600, ±370, and ±50 nm rms amplitude aberrations. Fig. 5 represents the fitted linear amplitude of the modal measurements and is a straight line with less than 0.1% error, this number not being meaningful as we may be limited here by our sensor. Fig. 6 shows the spatial deviation to this linear model (in pixel rms from SH slopes). The maximal spatial deviation to the linear model is 6 nm rms for mode #30, 10 nm rms for mode #300 and <5 nm rms for the last. The linearity of the DM is thus extremely good and again actually at the limit of the WFS measurements (<5 nm rms).

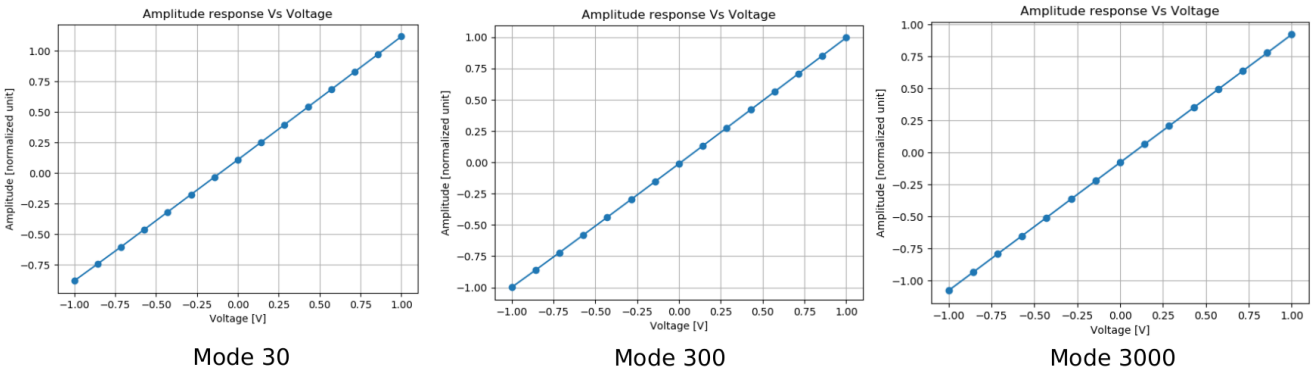

Mode 30 Mode 300 Mode 3000

Figure 5: Linearity curves for modes 30 (left), 300 (center), 3000 (right). The amplitude range is ±600 nm rms for mode #30, ±370 nm rms for mode #300 and ±50 nm rms for mode #3000.

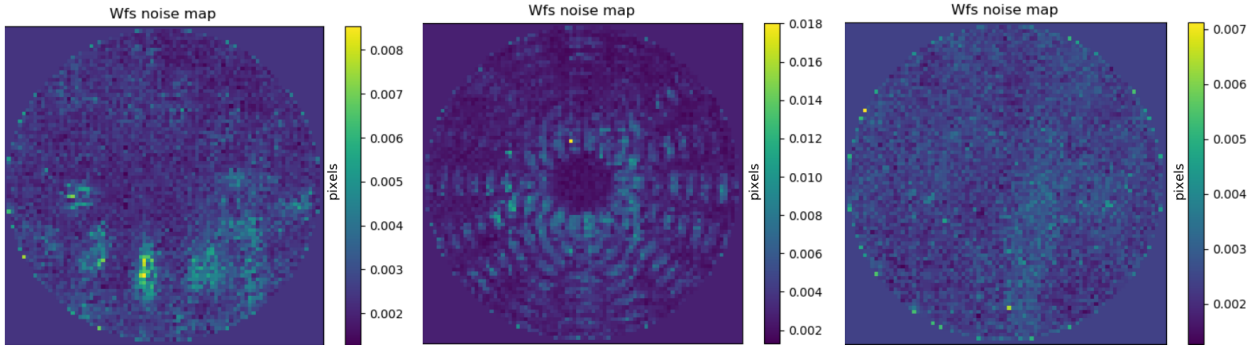

Mode 30 Mode 300 Mode 3000

Figure 6: Spatial deviation to DM linear model (i.e to the measured interaction matrix) for modes 30 (left), 300 (center) and 3000 (right). Color units are expressed in pixels. The maximum spatial deviation is for mode #300 is: 0.018px×739nm/px = 13nm rms (i.e 3% error)

5.4 Additivity

Additivity is the ability of the DM to behave as linear algebra would predict. Mathematically speaking, this should be named *linearity* but this would be confusing compared to the previous paragraph. Additivity is the property that any linear combination of commands will produce the same linear combination of wave-fronts.

In order to check this, we have recorded interaction matrices made by the sine wave method by varying the frequencies of each mode, and we also performed the interaction matrix by blocks of modes with variable composition. The result is simple: the difference between two interaction matrices achieved in very different conditions of modal composition is the same as the difference between two strictly identical realisations of the same matrix. In a word, the additivity error is smaller than the precision of our measurements, which is of the order of 5 nm rms.

5.5 Hysteresis

The principle for measuring the hysteresis is to modally poke the DM back and forth a number of times (usually 10) between two values, and get the associated measurements. The latter are processed exactly as in the case of linearity measurements described in the previous paragraph. The hysteresis cycle is shown as the *deviation* of the measured value to linearity, as a function of the applied value. Indeed, the level of hysteresis is so low that the tiny cycle is invisible when plotting the whole hysteresis graph: it only becomes observable when the average slope is subtracted.

On low and medium order modes (30, 300) the hysteresis is below <1% (Fig. 7) of the applied value, which is excellent. The performance is even better as the mode order increases, mode number 3000 is measured as low as <0.2% (see Fig. 7).

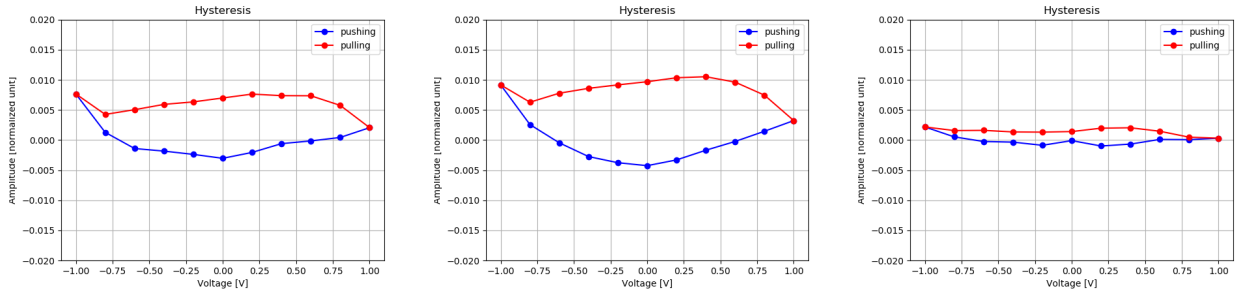

Figure 7: Hysteresis curves for modes #30 (left), #300 (center) and #3000 (right). The overall linearity response has been subtracted in order to magnify and make visible the hysteresis effect.

However, to be fair we have to say that the ensemble of results are not fully consistent within each others, and we ended up to the conclusion that the level of hysteresis is dependent from the time spent to measure the cycle. In the end, we are not fully convinced that hysteresis has been measured. Instead this apparent hysteresis could just be a consequence of a creeping effect, which is significant, and described in the next section. If this assumption is exact, then the hysteresis level is even smaller than the number we gave.

5.6 Creep

Creep effect is the tendency of a material to move slowly and deform under the influence of a permanent mechanical stress. Creep increases logarithmically with time following the relationship:

$$z(t) \approx z(t_0)\,(1 + g.\log(t/t_0)) \quad , \tag{14}$$

where z is the position/amplitude at time t and g is the creeping factor.

Fig. 8 represents the short term creep when applying the same shape during 3 seconds. It shows multiple ($\times$28) short term cycles of 3 second holding the same shape, and a zoom of one of these cycles, where the creep

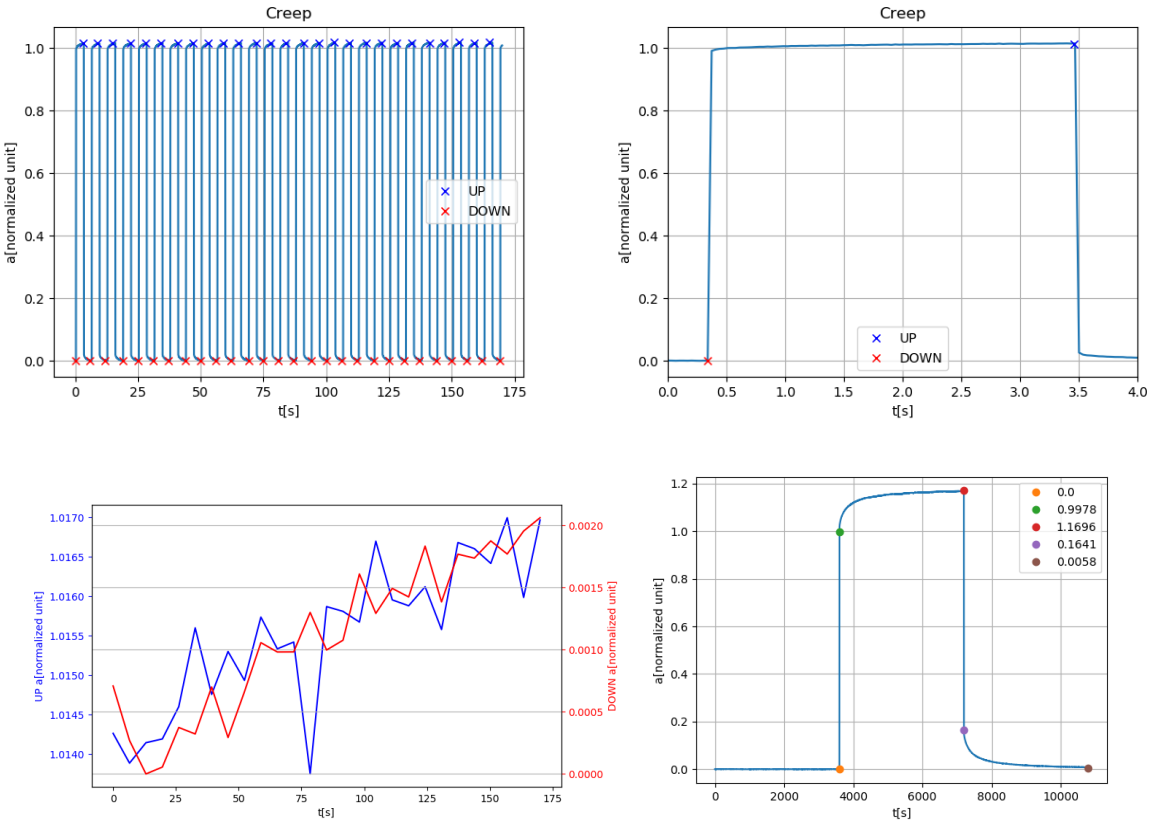

Figure 8: Top left: representation of 28 cycles of push-release sequences of 3s for mode #30. Top right: zoom on a single cycle of 3 seconds. Bottom left: Drift of the pushed position (blue) and zeros (released in red) across the 28 cycles, that exhibits a creeping tendency due to the fact that the cycle average is not 0. Bottom right: Long-term (1 hour) creep measured over 3 hours, up and down.

is visible at the top as a gentle increasing drift of the maximum value. The same effect could be visible for the bottom part of the cycle, right after the descent, the DM keeps some "memory" of the shape previously applied, and take some time to go back to 0. The figure in the middle and bottom of Fig. 8 represents the measured DM position at the end of the rising (blue) and descending (red) time for each of the 28 cycles. It shows that on top of the series of cycles where creep is observable on each of them, an overall creeping effect superimposes due to the fact that the average of the cycles is not null. The overall drift after those 28 cycles (175 seconds) is 0.2%.

Figure 8 (bottom right) also shows the measured creeping effect when applying a constant shape of mode #30 and holding it one hour, and finally resetting the command and observe one hour more. We measured after 3600 s a position of ≈1.17 (from a normalized value at t_0 of 1) leading to a creep factor of ≈0.02 which is an average value (usually in the range of [0.01-0.03]).

5.7 Conclusion

The ALPAO 64×64 deformable mirror is currently in our lab for tests since the beginning of April 2019. The DM characteristics are so far promising although we did not started to measure its temporal dynamics yet. The DM static components are very good, in particular, it features a perfect modal additivity and linearity response, a very low hysteresis and low creep/drift effect. We found the stroke slightly limited for being used as a first turbulence correction stage on a 40m telescope class due to the electronics energy saturation management, however this DM is perfectly well suited for being used on a 8-10m telescope class. Next steps will focus on the measurement of the DM temporal response and open loop tests in the framework of the MOSAIC instrument.

ACKNOWLEDGMENTS

The deformable mirror presented in this paper has been funded by a grant from DIM ACAV/Région Ile-de-France and thanks to the financial support of INSU. This work was also supported by INSU and Observatoire de Paris through the funding of J. Raffard's position.

REFERENCES

[1] Davies, R., Schubert, J., Hartl, M., Alves, J., Clénet, Y. et al., "MICADO: first light imager for the E-ELT", Proceedings of the SPIE, Volume 9908, id. 99081Z 12 pp. (2016)

[2] Clénet, Y. and Buey, T. and Gendron, E. and Hubert, Z. and Vidal, F. and others "MICADO-MAORY SCAO: preliminary design, development plan & calibration strategies", 6th AO4ELT conference-Adaptive Optics for Extremely Large Telescopes held in Quebec (2019)

[3] Mahiou P., Laslandes M. and Charton J. , "New deformable Mirrors available for the ELT and future developments", AO4ELT6 conference proceedings held in Quebec (2019)

[4] Kasper M. and Fedrigo E., "Fast calibration of high-order adaptive optics systems", J. Opt. Soc. Am. A/Vol. 21, No. 6 (2004)

[5] Meimon S., Petit C., Fusco T., "Optimized calibration strategy for high order adaptive optics systems in closed-loop: the slope-oriented Hadamard actuation", Optics Express, Optical Society of America, 2015, 23 (21), pp.27134-27144. (2015)